

PAPER

# Generation of Circularly Polarized Strong-Field Terahertz Waves

To cite this article: Jiang-Hao Li *et al* 2024 *Chinese Phys. Lett.* **41** 124201

View the [article online](#) for updates and enhancements.

## You may also like

- [Pentameric Assembly Architecture of the Tail Tube Protein in SPR Phages](#)  
Lin Wang, Yuhang He, Kaixiang Zhu et al.
- [Systematic Uncertainties from Gribov Copies in Lattice Calculation of Parton Distributions in the Coulomb Gauge](#)  
Xiang Gao, Jinchen He, Rui Zhang et al.
- [Enhanced Coupling of Superconductivity and Evolution of the Gap Structure in CsV<sub>3</sub>Sb<sub>5</sub> via Ta Doping](#)  
Yiwen Li, , Zhengyan Zhu et al.

## Generation of Circularly Polarized Strong-Field Terahertz Waves

Jiang-Hao Li(李江皓)<sup>1†</sup>, Hong-Ting Xiong(熊虹婷)<sup>1†</sup>, De-Yin Kong(孔德胤)<sup>1,2</sup>, Wei-Peng Zhao(赵蔚鹏)<sup>1</sup>, Shao-Jie Liu(刘少杰)<sup>3</sup>, Bao-Gang Quan(全保刚)<sup>4,5,6</sup>, and Xiao-Jun Wu(吴晓君)<sup>1,2,7,8\*</sup>

<sup>1</sup>*School of Electronic and Information Engineering, Beihang University, Beijing 100191, China*

<sup>2</sup>*Zhangjiang Laboratory, Shanghai 201210, China*

<sup>3</sup>*Department of Physics, Hong Kong University of Science and Technology, Hong Kong, China*

<sup>4</sup>*Beijing National Laboratory for Condensed Matter Physics, Institute of Physics, Chinese Academy of Sciences, Beijing 100190, China*

<sup>5</sup>*Songshan Lake Material Laboratory, Guangdong 523808, China*

<sup>6</sup>*University of Chinese Academy of Sciences, Beijing 100049, China*

<sup>7</sup>*Wuhan National Laboratory for Optoelectronics, Huazhong University of Science and Technology, Wuhan 430074, China*

<sup>8</sup>*International Terahertz Research Center, Hangzhou International Innovation Institute, Beihang University, Hangzhou 311115, China*

(Received 23 August 2024; accepted manuscript online 25 October 2024)

Terahertz (THz) circular dichroism (TCD) spectroscopy is extensively used to examine the chiral properties of biological macromolecules and other materials. The rapid advancements in strong-field THz generation and field-modulated techniques highlights the importance of advancing tunable strong-field TCD spectroscopy technology. In this study, we designed and implemented an integrated strong-field TCD spectroscopy system. By using a tilted-pulse-front technique, we generated linearly polarized strong-field THz radiation and achieved linear-to-circular polarization conversion via a reflective metasurface. The resulting circularly polarized THz radiation exhibited an ellipticity greater than 0.9 in the frequency range of 0.38–0.61 THz, achieving a linear-to-circular conversion efficiency exceeding 90%. Additionally, the peak electric field strength of the circularly polarized THz radiation exceeded 100 kV/cm. The proposed system is expected to be instrumental in investigating the chiral characteristics of materials under strong field conditions and in examining how these characteristics vary under different field conditions.

DOI: [10.1088/0256-307X/41/12/124201](https://doi.org/10.1088/0256-307X/41/12/124201)

Circular dichroism (CD) spectroscopy characterizes chirality by measuring a material's differential absorption of left- and right-handed circularly polarized (LCP and RCP) waves. Biological macromolecules such as proteins exhibit strong CD signals in the terahertz (THz) frequency range,<sup>[1,2]</sup> making CD spectroscopy crucial for determining chiral structures,<sup>[3]</sup> studying macromolecular dynamics,<sup>[4]</sup> cell sensing,<sup>[5]</sup> and distinguishing between biological and non-biological materials.<sup>[6]</sup> In condensed matter physics, certain quantum materials may display chiral responses to circularly polarized THz (CP-THz) radiation.<sup>[7]</sup> Recent research has also focused on manipulating phonons in materials using circularly polarized THz light to control their magnetic properties.<sup>[8–10]</sup> Moreover, advancements in strong-field THz technology<sup>[11–14]</sup> have facilitated investigations into THz-induced effects, such as non-thermal effects in biological systems,<sup>[15]</sup> ultrafast THz thermochemistry,<sup>[16]</sup> and field-modulated nonlinear metasurfaces.<sup>[17]</sup> However, exploring the modulation of the materials' chirality under varying field strengths remains notable yet challenging for traditional weak-field terahertz

CD (TCD) systems.

Generating strong-field CP-THz radiation poses additional challenges. Existing methods, such as femtosecond laser pumping in materials like InAs,<sup>[18]</sup> GaP,<sup>[19]</sup> NiO,<sup>[20]</sup> and spintronic emitters,<sup>[21–25]</sup> often fail to achieve high electric field intensities. Although laser-driven, two-color air plasma sources provide higher field strengths, they suffer from system complexity and relatively low signal-to-noise ratios (SNR).<sup>[26]</sup> Furthermore, linear-to-circular (LTC) THz wave conversion through transmissive elements like quarter-wave plates<sup>[27]</sup> faces challenges related to the thickness-dependent bandwidth and transmission losses. Recently, metasurfaces have emerged as a promising approach for achieving broadband, high-efficiency LTC conversion.<sup>[28–30]</sup> Researchers have actively addressed the challenges related to bandwidth limitations, loss, and dispersion. For instance, Ref. [31] proposed a feasible metasurface design based on coupled mode theory to achieve broadband LTC conversion, achieving nearly 100% LTC conversion efficiency over a substantial bandwidth under weak-field conditions.

<sup>†</sup>These authors contributed equally to this work.

\*Corresponding author. Email: xiaojunwu@buaa.edu.cn

© 2024 Chinese Physical Society and IOP Publishing Ltd

In this study, we constructed a strong-field TCD spectroscopy system. Using the tilted-pulse-front technique, linearly polarized strong-field THz radiation was generated with a peak electric field of 150 kV/cm. We achieved RCP and LCP strong-field THz waves with the LTC metasurface device, which exhibited ellipticity greater than 0.9 over a broad frequency range (0.3–0.6 THz). The LTC conversion efficiency exceeded 90%, and the maximum electric field strength of both the LCP and RCP waves exceeded 100 kV/cm, facilitating the study of chiral characteristics under varying field intensities.

We employed a birefringent reflective metasurface to achieve LTC polarization conversion, taking advantage of its enhanced THz energy efficiency by reducing the transmission loss compared to its transmissive counterparts.

Based on coupled mode theory,<sup>[32]</sup> the metasurface design compensates for the frequency dependence of the birefringent phase dispersion by introducing resonance peaks and adjusting the phase dispersion curve at nonresonant frequencies. The unit structure of the metasurface is illustrated in Fig. 1(a). The incident electric field was decomposed into two orthogonal components ( $E_{\perp}$  and  $E_{\parallel}$ ) based on the polarization direction relative to the longer side of the Si pillars. The perpendicular component  $E_{\perp}$  primarily underwent planar reflection with linear phase dispersion, whereas the parallel component  $E_{\parallel}$  experienced strong reflection from both the resonator and the plane. The gaps between the high-resistivity Si pillars form Fabry-Pérot resonators, creating an underdamped resonance for dispersion compensation.

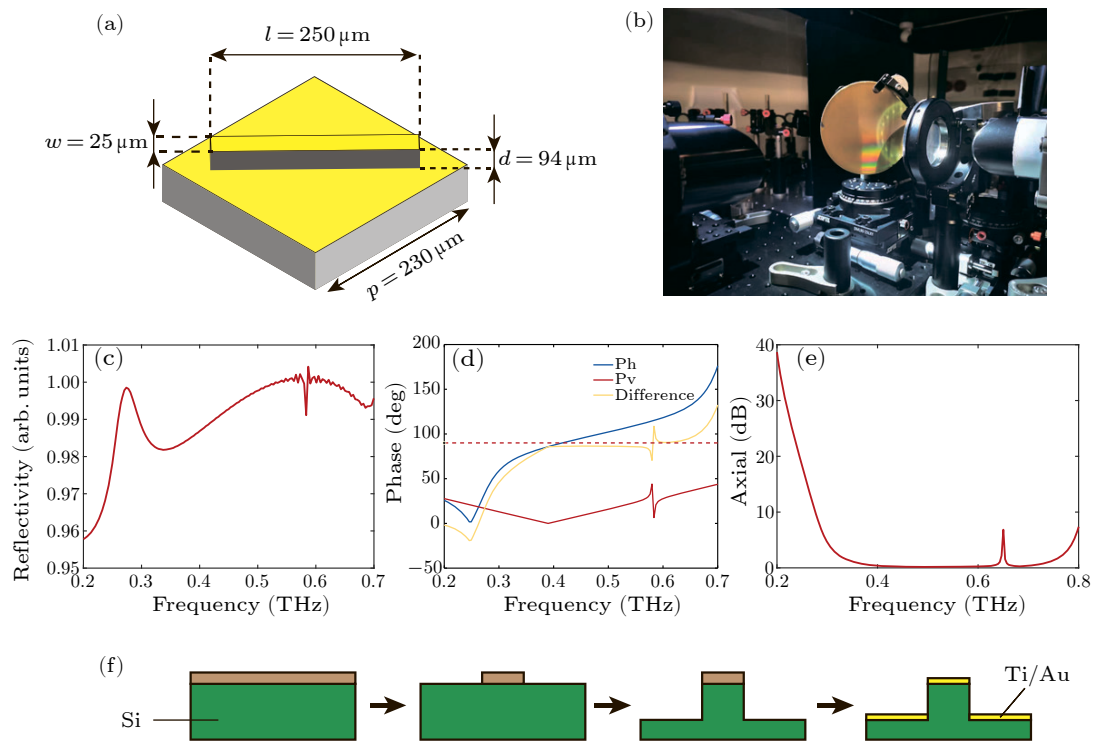


**Fig. 1.** Linear-to-circular conversion THz metasurface. (a) Schematic of the metasurface unit structure; (b) a 4-inch metasurface positioned in the optical path. Electromagnetic simulation results: (c) energy reflectivity, (d) phase difference, and (e) axial ratio. (f) Fabrication process of the metasurface.

The specific design parameters of the metasurface are labeled in Fig. 1(a), targeting the frequency range of 0.3–0.55 THz, which corresponds to the central frequency range of the THz source used. The square lattice period is 230  $\mu\text{m}$ ; the rectangular Si pillar length has a length of 250  $\mu\text{m}$ , a width of 25  $\mu\text{m}$ , and a height of 94  $\mu\text{m}$  (etch depth of the Si). Analyzing the simulation results in Figs. 1(c)–1(e), we observed that within the 0.3–0.56 THz frequency range, the device’s reflectivity remained above 0.98; the phase difference fluctuates within 10% around a target value of  $90^\circ\pi/2$ , and the axial ratio is below 0.1 dB. A phase difference close to  $90^\circ$  improves the ellipticity of the reflected THz waves, whereas a stable phase difference

contributes to reduced dispersion in the fabricated metasurface. These results indicate that the device can theoretically convert linearly polarized THz waves into the desired circularly polarized waves efficiently within the target frequency range.

The fabrication process of the metasurface is shown in Fig. 1(f). First, a photoresist layer was spin-coated onto the surface of a high-resistivity Si substrate to serve as an etching mask. This was followed by deep silicon ion etching to create the rectangular Si pillar array. After removing the photoresist, a Ti/Au film with a thickness of 10/200 nm was deposited onto the sample surface using electron beam evaporation. The Au layer enhances THz

reflectivity, while the Ti layer ensures adhesion between the Au and Si substrate. The fabricated device is shown in Fig. 1(b).

Using the metasurface, we developed the optical path for strong-field THz CD spectroscopy system, as shown in Fig. 2. Laser pulses generated from a femtosecond laser amplifier (operating wavelength: 800 nm, repetition rate: 1 kHz, pulse width: 35 fs, and output power:  $\sim 5$  W) were used to pump the LiNbO<sub>3</sub> crystal, producing vertically polarized strong-field THz waves. The pulse width was adjusted to achieve a peak frequency of approximately 0.45 THz, focusing the energy distribution more toward lower frequencies (spectrum shown in the Supplementary Material). Before the incident beam reaches the crystal, it is reflected by a grating to create a tilted-pulse-front.

The strong-field THz emission exiting the LiNbO<sub>3</sub> crystal is reflected by a silver mirror and collected by an off-axis parabolic mirror (OAP1). After reflection by the LTC conversion metasurface, the linearly polarized, parallel THz beam is converted to CP-THz. The maximum THz electric field strength was achieved at the focal point between OAP2 and OAP3. Polarizers P3 and P4 were positioned between OAP3 and OAP4, with P3 adjusted to  $+45^\circ$  and  $-45^\circ$  during measurement to collect the  $E_x$  and  $E_y$  components of the CP-THz radiation, respectively. P4

ensures that the THz electric field direction aligns with the crystal axis of the electro-optic crystal. A 500- $\mu\text{m}$ -thick  $\langle 110 \rangle$  ZnTe crystal is used as the electro-optic crystal. After THz reflection by OAP4, the THz and probe light were co-focused on the ZnTe crystal, and the THz time-domain waveform was obtained via electro-optic sampling method.

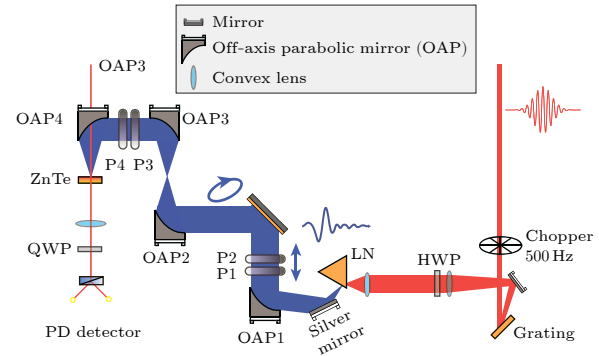


**Fig. 2.** Strong-field terahertz (THz) circular dichroism spectroscopy system. The red and blue lines represent the 800-nm laser path and THz wave path, respectively. The arrows indicate the polarization states of the THz waves. P1–P4 denote the four THz polarizers in optical path order. Here, LN denotes the LiNbO<sub>3</sub> crystal, and HWP and QWP refer to the half-wave and quarter-wave plates, respectively.

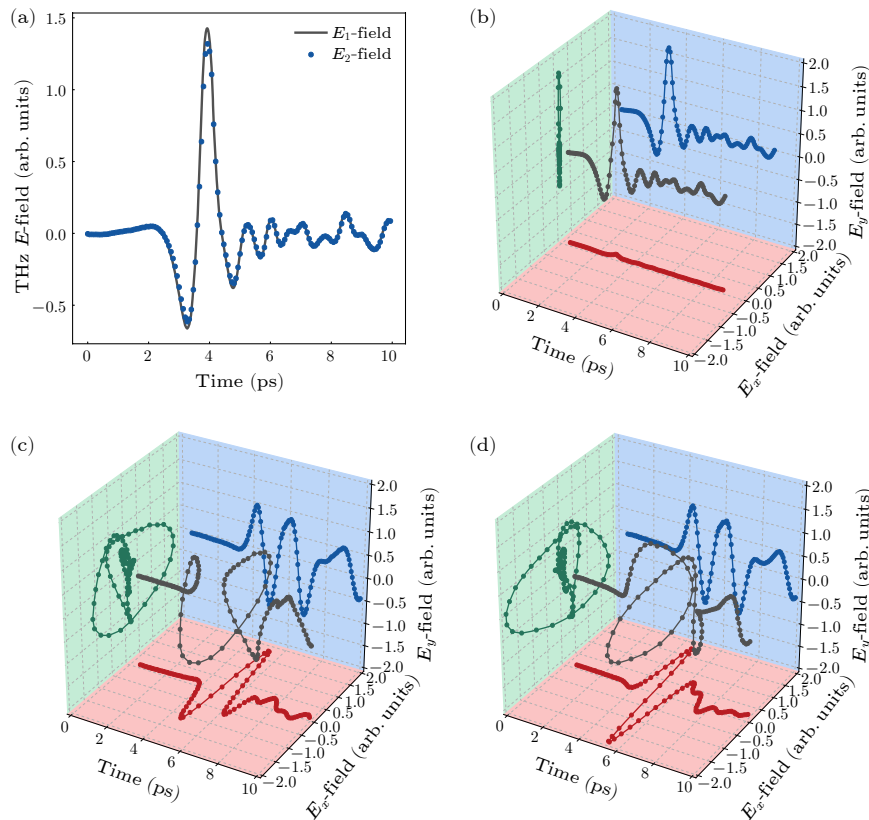


**Fig. 3.** Generation of circularly polarized terahertz (CP-THz) waves. (a) Signals  $E_{10}$  and  $E_{20}$  obtained with the reference sample in place, with P1 and P2 oriented vertically to align with the polarization of the incident THz waves. (b) System reference signals indicate predominantly linear polarization. (c) Generated right-handed circularly polarized THz waveform with the incident THz polarization and metasurface orientation at  $-45^\circ$ . (d) Generated left-handed circularly polarized THz waveform with the angle set to  $+45^\circ$ .

Let the time-domain electric field signals obtained at P3 orientation angles of  $+45^\circ$  and  $-45^\circ$  be  $E_1$  and  $E_2$ , respectively. The electric field components  $E_x$  and  $E_y$  can then be calculated using the following relationships:

$$E_x \propto E_1 + E_2, \quad (1)$$

$$E_y \propto E_1 - E_2. \quad (2)$$

The reference sample, a Ti/Au film layer on the Si substrate, was placed at the LTC conversion metasurface (LTC position) to precisely adjust the system. While maintaining the vertical orientations of P1, P2, and P4, the polarizer P3 was adjusted to  $+45^\circ$  and  $-45^\circ$  to collect the reference time-domain signals  $E_{10}$  and  $E_{20}$ . These two signals are illustrated in Fig. 3(a), where the solid gray and blue dots represent the data points of both signals. The peak values of the two signals were approximately equal, confirming that the LTC position was correctly aligned. The polarized electric field components  $E_x$  and  $E_y$ , extracted from  $E_{10}$  and  $E_{20}$ , along with the system reference signal are depicted in Fig. 3(b). The THz waves were primarily linearly polarized, indicating that the substrate had minimal effect on the ellipticity of the generated CP-THz. The entire experiment was conducted in ambient air

without nitrogen or dry air purging at a relative humidity of about 40%.

After the adjustment, we replaced the reference sample with the LTC conversion metasurface. The THz energy reflectivity of the metasurface was measured at approximately 95.12% (details of the method and optical path are provided in the Supplementary Material). Vertically polarized THz waves were directed onto the metasurface, with the linear polarization direction forming a  $-45^\circ$  angle relative to the metasurface's grating structure. As with the reference signal, P3 was adjusted to  $+45^\circ$  and  $-45^\circ$  to obtain  $E_{1,RCP}$  and  $E_{2,RCP}$ . The two polarized electric field components,  $E_x$  and  $E_y$ , were calculated using Eqs. (1) and (2). The synthesized THz waveform is shown in Fig. 3(c), with its projection in the YOZ plane confirming the generation of RCP THz waves. By rotating polarizer P2 clockwise by  $90^\circ$  so that the polarization direction of the incident THz waves forms a  $+45^\circ$  angle with the Si pillars, LCP THz waves were obtained, as depicted in Fig. 3(d). Additionally, by adjusting the angle of the polarizer or the metasurface, elliptically polarized waves can also be generated if needed.

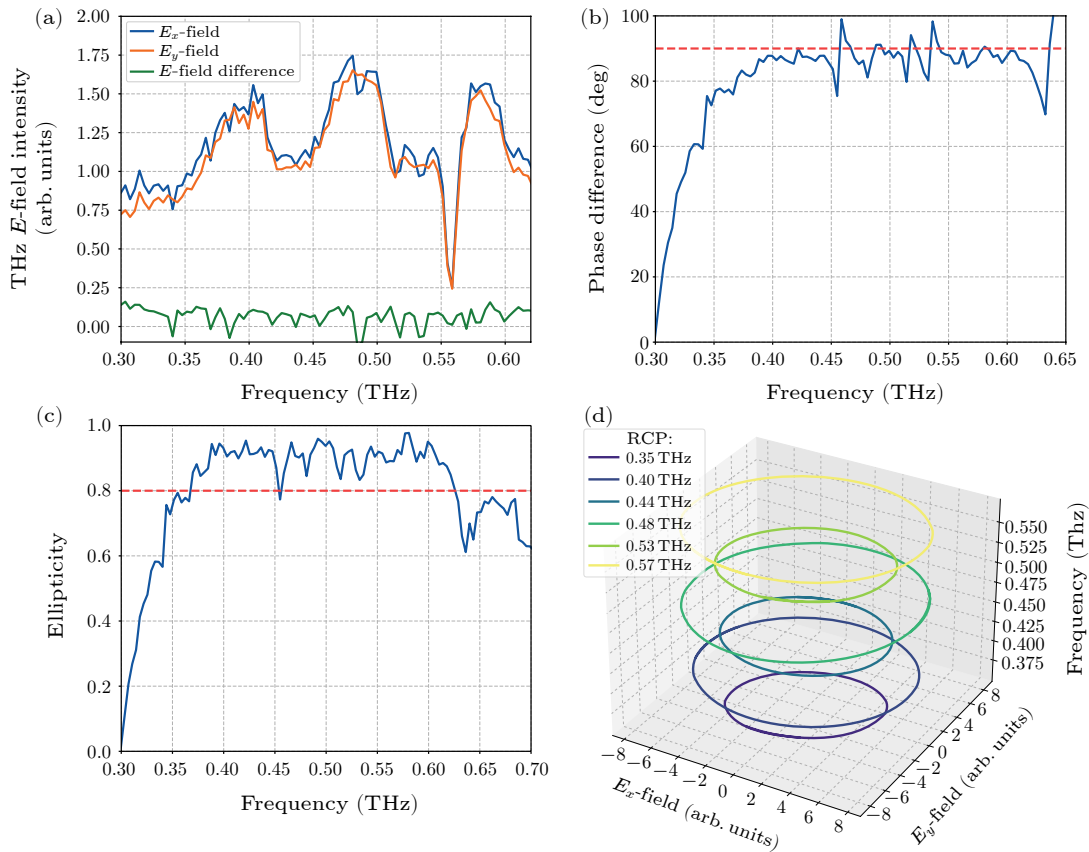


**Fig. 4.** Detailed characteristics of the generated right-handed circularly polarized terahertz (RCP THz) waves. (a) Frequency spectra of  $E_x$ ,  $E_y$ , and their difference. (b) Phase difference between  $E_x$  and  $E_y$ . (c) Ellipticity curve of the RCP waves. (d) CP-THz electric field vector diagrams at several frequencies.

We use the RCP waves as an example to further quantify the obtained CP-THz waves. The two orthogonal electric field components can be expressed using Eqs. (3) and

(4) as follows:

$$E_x = a_x \cos(\omega t + \varphi_x), \quad (3)$$

$$E_y = a_y \cos(\omega t + \varphi_y). \quad (4)$$

By applying the fast Fourier transform algorithm to the electric field components  $E_x$  and  $E_y$ , we obtained their respective spectral information. The amplitude spectra are shown in Fig. 4(a). It can be observed that the two electric field components are nearly identical, with  $E_x$  slightly larger than  $E_y$  by approximately 3.8%. A substantial signal drop near 0.55 THz corresponds to water vapor absorption, confirming the system's high SNR to a certain extent. Figure 4(b) shows the phase difference spectrum  $\Delta\varphi = \varphi_x - \varphi_y$  between  $E_x$  and  $E_y$  components, with the red dashed line indicating a  $90^\circ$  phase difference. In the range of 0.3–0.37 THz, the phase difference increases rapidly from  $0^\circ$  to  $80^\circ$  and remains around  $90^\circ$  between 0.4 and 0.6 THz. The unsmoothed experimental results align well with the simulated results shown in Fig. 1(d), demonstrating minimal dispersion across this frequency range.

From the forms of Eqs. (3) and (4), we derived the mathematical expression for ellipticity in terms of the amplitudes and phase differences of the two orthogonal components, as shown in Eq. (5):

$$\eta = \frac{a}{b} = \sqrt{\frac{a_x^2 + a_y^2 - \sqrt{4a_x^2 a_y^2 \cos^2 \Delta\varphi + (a_x^2 - a_y^2)^2}}{a_x^2 + a_y^2 + \sqrt{4a_x^2 a_y^2 \cos^2 \Delta\varphi + (a_x^2 - a_y^2)^2}}}. \quad (5)$$

Figure 4(c) shows the calculated ellipticity curve. In the frequency range 0.37–0.63 THz, the ellipticity remained above 0.8, exceeding 0.9 in the 0.38–0.61 THz range. To more intuitively visualize the generated CP-THz electric field, THz electric field vector diagrams at selected frequency points were plotted based on the endpoints of the THz electric field vectors, as shown in Fig. 4(d).

We also calculated the peak electric field intensity of the generated CP-THz radiation. The calculation method is similar to linearly polarized THz radiation (as described in Ref. [33]) and is detailed in the Supplementary Material. For RCP, the calculated peak electric field strength of the circularly polarized electric field was  $E_{\text{RCP}} = 113.53$  kV/cm, with an energy conversion efficiency from LTC polarization of approximately 93.88%. Similarly, for LCP, the calculated peak electric field strength was  $E_{\text{LCP}} = 100.18$  kV/cm.

In summary, we combined a LiNbO<sub>3</sub> strong-field THz source with an LTC metasurface device to construct a strong-field THz CD spectroscopy system. Experimentally, we generated RCP and LCP strong-field THz radiation across a frequency range of 0.3–0.6 THz, achieving an ellipticity above 0.9 and a peak electric field intensity exceeding 100 kV/cm. Our system shows substantial potential for studying the chiral properties of materials under strong-field conditions and examining the dependence of material chirality on field strength.

**Acknowledgements.** This work was supported by the National Key R&D Program of China under Grant No. 2022YFA1604402, the National Natural Science Foundation of China under Grant Nos. U23A6002 and 92250307, and the Open Project Program of Wuhan National Laboratory for Optoelectronics under Grant No. 2022WNLOKF006.

## References

- [1] Acbas G, Niessen K A, Snell E H *et al.* 2014 *Nat. commun.* **5** 3076
- [2] Zhang Z Y, Fan F, Shi W N *et al.* 2022 *Biomed. Opt. Express* **13** 209
- [3] Choi W J, Lee S H, Park B C *et al.* 2022 *J. Am. Chem. Soc.* **144** 22789
- [4] King M D, Buchanan W D, and Korter T M 2011 *Journal of pharmaceutical sciences* **100** 1116
- [5] Zhang Z Y, Yang G, Fan F *et al.* 2021 *Analytica Chimica Acta* **1180** 338871
- [6] Xu J, Ramian G J, Galan J F *et al.* 2003 *Astrobiology* **3** 489
- [7] Jasper E V, Mai T T, Warren M T *et al.* 2020 *Phys. Rev. Mater.* **4** 013803
- [8] Luo J M, Lin T, Zhang J J *et al.* 2023 *Science* **382** 698
- [9] Basini M, Pancaldi M, Wehinger B *et al.* 2024 *Nature* **628** 534
- [10] Geilhufe R M and Hergert W 2023 *Phys. Rev. B* **107** L020406
- [11] Wu X J, Ma J L, Zhang B L *et al.* 2018 *Opt. Express* **26** 7107
- [12] Fülöp J A, Tzortzakis S, and Kampfrath T 2020 *Advanced Optical Materials* **8** 1900681
- [13] Wu X J, Kong D Y, Hao S B *et al.* 2023 *Advanced Materials* **35** 2208947
- [14] Zhang B L, Li Y F, Wu X J *et al.* 2024 *Laser & Photonics Reviews* **18** 2300895
- [15] Wilmink G J and Grundt J E 2011 *Journal of Infrared, Millimeter, and Terahertz Waves* **32** 1074
- [16] Allodi M A, Finneran I A, and Blake G A 2015 *The Journal of Chemical Physics* **143** 234204
- [17] Cai J H, Chen S, Geng C Y *et al.* 2023 *Nanophotonics* **12** 2517
- [18] Sarukura N, Ohtake H, Izumida S *et al.* 1998 *J. Appl. Phys.* **84** 654
- [19] Sato M, Higuchi T, Kanda N *et al.* 2013 *Nature Photonics* **7** 724
- [20] Kanda N, Higuchi T, Shimizu H *et al.* 2011 *Nat. Commun.* **2** 362
- [21] Chen X H, Wu X J, Shan S Y *et al.* 2019 *Appl. Phys. Lett.* **115** 221104
- [22] Zhao H H, Chen X H, Ouyang C *et al.* 2020 *Advanced Photonics* **2** 066003
- [23] Chen X H, Wang H T, Wang C *et al.* 2021 *Advanced Photonics Research* **2** 2000099
- [24] Kong D Y, Wu X J, Wang B *et al.* 2019 *Advanced Optical Materials* **7** 1900487
- [25] Li P Y, Liu S J, Chen X H *et al.* 2022 *Frontiers of Optoelectronics* **15** 12
- [26] Tailliez C, Stathopoulos A, Skupin S *et al.* 2020 *New J. Phys.* **22** 103038
- [27] Masson J B and Gallot G 2006 *Optics letters* **31** 265
- [28] Grady N K, Heyes J E, Chowdhury D R *et al.* 2013 *Science* **340** 1304
- [29] Choi W J, Cheng G, Huang Z *et al.* 2019 *Nature materials* **18** 820
- [30] Peralta X G, Smirnova E I, Azad A K *et al.* 2009 *Optics express* **17** 773
- [31] Hao J M, Yuan Y, Ran L X *et al.* 2007 *Phys. Rev. Lett.* **99** 063908
- [32] Chang C C, Zhao Z X, Li D F *et al.* 2019 *Phys. Rev. Lett.* **123** 237401
- [33] Zhang B L, Ma Z Z, Ma J L *et al.* 2021 *Laser & Photonics Reviews* **15** 2000295